Microfluidics and Nanofluidics (2019) 23:135
https://doi.org/10.1007/s10404-019-2301-3

RESEARCH PAPER

Inertia-magnetic particle sorting in microfluidic devices: a numerical parametric investigation

Mohammad Charjouei Moghadam[1] · **Armin Eilaghi**[2] · **Pouya Rezai**[1]

Received: 23 September 2019 / Accepted: 2 November 2019 / Published online: 20 November 2019

Abstract

Microfluidic-based sorting systems are an integral part of many biological applications, where sorting of cells, microorganisms, and particles is of interest. In this paper, a computational fluid dynamics model is established to expand investigations on a hybrid microparticle sorting method, which combines inertia-magnetic focusing and hydrodynamic separation, known as multiplex inertia-magnetic fractionation (MIMF). This microfluidic device consists of two regions, i.e. a narrow microchannel with a magnet on its side for inertial and magnetophoretic focusing of particles and a downstream wide hydrodynamic expansion zone for particles' separation and imaging. A Lagrangian–Eulerian framework was adopted to simulate particle trajectories using the ANSYS-Fluent discrete phase modeling (DPM) approach. Acting forces that were considered to predict particle trajectories included the drag, inertial lift, Saffman lift, gravitational, and magnetophoretic forces. User-defined functions were used for inertial lift and magnetophoretic forces that are not built-in relations in the ANSYS-Fluent DPM. Numerical results were verified and validated against the experimental data for MIMF of 5 and 11 μm magnetic particles at flow rates of 0.5–5 mL/h. Particles fractionation throughput and purity in the expansion region could be predicted with errors of 6% and 2%, respectfully. The validated model was then used to perform a numerical parametric study on the unknown effects of magnetization, particle size, higher flow rates, and fluid viscosity on MIMF. The presented numerical approach can be used as a tool for future experimental design of inertia-magnetophoretic microfluidic particle sorting devices.

Keywords Microfluidic sorting · Computational fluid dynamics · Magnetophoresis · Inertial focusing · Hydrodynamic fractionation · Discrete phase modeling

1 Introduction

Sorting and separation of small substances such as cells, microorganisms, and microparticles and nanoparticles from a heterogeneous mixture is a common sample preparation step in many biological applications such as diagnosis (Saliba et al. 2010), genomics (Podar et al. 2007; Yilmaz and Singh 2012), cellomics (Andersson and Van den Berg 2003), and immunoassays (Cheng et al. 2018). Particle and cell sorting are normally performed by laboratory-based methodologies that involve sedimentation, filtration, or centrifugation. These conventional methods are time-consuming, prone to filter clogging, and expensive. Other commonly used methods such as fluorescence-activated cell sorting (Geens et al. 2006; Julius et al. 1972) and magnetic-activated cell sorting (Adams et al. 2008) are more accurate and specific to target cells. But they require compatibility with fluorescent tagging and in-line fluorescent imaging, analysis and downstream sorting that makes them costly, complex, and inaccessible, especially for point-of-care and point-of-use applications.

An ideal sorting method must meet certain requirements such as involving a simple and low-cost design, working continuously at high throughput, being efficient in terms of energy consumption, operating without a diluting sheath flow and performing multiplex separation with high purity and efficiency (Kumar and Rezai 2017a). Recently, many

Electronic supplementary material The online version of this article (https://doi.org/10.1007/s10404-019-2301-3) contains supplementary material, which is available to authorized users.

✉ Pouya Rezai
prezai@yorku.ca

1 Department of Mechanical Engineering, York University, BRG 433B, 4700 Keele St, Toronto, ON M3J 1P3, Canada

2 Department of Mechanical Engineering, Australian College of Kuwait, Kuwait City, Kuwait

biological applications such as cancer diagnosis (Chen et al. 2012; Karabacak et al. 2014; Lee et al. 2013; Nagrath et al. 2007; Ozkumur et al. 2013; Pappas 2016), immunomagnetic assays (Dalili et al. 2019; Ng et al. 2010), and pathogen separation (Bayat and Rezai 2018; Jiang et al. 2016; Ramadan et al. 2010; Richardson and Ternes 2011) have benefitted from microfluidic-based sorting systems that meet most of the requirements above and exceed expectations by offering minimal reagent consumption and portability (Baker et al. 2009; Bélanger and Marois 2001).

Several microfluidic particle sorting methods have been proposed such as pinched flow fractionation (Wang et al. 2005; Yamada et al. 2004), hydrodynamic filtration (Yamada and Seki 2005), deterministic lateral displacement (Huang et al. 2004), size exclusion filtration (Mohamed et al. 2007), optical sorting (Applegate et al. 2006), dielectrophoresis (Valero et al. 2010; Zhang et al. 2018), acoustic separation (Li et al. 2015), and magnetophoresis (Chalmers et al. 1998). Samples are flown hydrodynamically in microchannels, while target particles are separated from nontargets either via the use of flow-induced passive forces such as inertial and drag or actively using magnetic, electrokinetic, acoustic, and optical stimuli (Wyatt Shields Iv et al. 2015).

Among the active microfluidic sorting methods, magnetophoretic sorting with permanent magnets has attracted a lot of attention due to its semi-passive nature, yet specificity and high precision in sorting target biomarkers (Saeed et al. 2014; Sajeesh and Sen 2014; Wyatt Shields Iv et al. 2015). Nevertheless, design of a robust sorting device remains challenging as some of these methods are developed by experimental trial and error that is costly and time consuming (Hejazian et al. 2015; Hoffmann et al. 2002; Krishnan et al. 2009; Kumar and Rezai 2017a, b; Martel and Toner 2014; Matas et al. 2004). Numerical methods have been adopted to facilitate the design of microfluidic-based sorting systems and expand rapidly on experimental outcomes, starting with simulating the motion of spherical particles in a fluid medium (Matas et al. 2004; Yang et al. 2005). Earlier models were mostly limited to either 2D domains or simple geometries (Feng et al. 1994a, b). Recently, more complex geometries such as straight, spiral, and T-shaped microchannels have been simulated (Bhagat et al. 2008; Modak et al. 2009). A major advantage is that these models can provide the capability to investigate the effect of multiple dominant forces on particle focusing and separation such as the combined effects of inertial focusing and magnetophoresis on magnetic particles.

Polyflow (Feng et al. 1994a, b) and CFD-ACE (Bhagat et al. 2008; Krishnan et al. 2009; Telleman et al. 1998) programs were among the popular numerical solvers employed. These solvers were abandoned due to their inability to accommodate the multi-physical complexity of the microfluidic-based sorting systems. COMSOL Multiphysics and ANSYS-Fluent are being adopted nowadays, as they cover a wide range of numerical analyses with accuracy and simplicity. For instance, in 2015, Amin (2014) performed a simulation on the effects of inertial focusing in a spiral microchannel with a trapezoidal cross section employing the discrete phase model (DPM) of ANSYS-Fluent. Particle trajectories were calculated considering the dominant forces acting on them, including the drag, buoyant, and lift forces. The lift force was included in the force balance through the addition of a user-defined function (UDF). A polynomial approximation based on the variations of the lift coefficient with Reynolds number was derived to predict the lift coefficient. In a more recent study, Parrot (2017) utilized a similar numerical framework and modified the proposed lift coefficient based on the particle distance from the sidewall rather than the Reynolds number.

Numerical studies on magnetophoretic microfluidic-based sorting systems, as one of the objectives in this paper, are scarce in the literature (Yang et al. 2016). Among the earlier studies, analytical models (Nandy et al. 2008; Zhu et al. 2011) and CFD-ACE + program (Krishnan et al. 2009) were adopted for simulation. Specialized numerical models (Modak et al. 2010; Zolgharni et al. 2007) have also been developed to simulate specific cases. Forbes and Forry (2012) developed a numerical model to investigate microfluidic magnetophoretic separation of immunomagnetically labeled rare mammalian cells. Their model accounts for the magnetic orientation, magnet type, flow rate, channel geometry, and buffer to achieve the desired level of magnetophoretic deflection or capturing. Hale and Darabi (2014) utilized COMSOL Multiphysics to simulate their magnetophoretic microfluidic device for DNA isolation and studied the effect of various parameters on the magnetic flux within a separation channel. In another study, Kim et al. (2016) proposed a numerical model that uses hydrodynamic viscous drag and magnetophoretic repulsion forces to predict particle trajectories. These efforts have certainly contributed to the numerical modeling of microfluidic-based sorting systems, however, to the best of our knowledge, a numerical framework that accounts for the effects of magnetophoretic focusing, inertial, and drag forces, as well as hydrodynamic fractionation is currently lacking.

The present study attempts to establish a 3D numerical framework to simulate our multiplex inertia-magnetic fractionation (MIMF) method proposed earlier (Kumar and Rezai 2017a, b). Standard Navier–Stokes equations were discretized and solved to simulate the flow. ANSYS-Fluent DPM was adapted to model particle trajectories and distribution in the microfluidic device. Acting forces on the particles such as drag, lift, gravitational, and magnetophoretic forces were considered to calculate particle trajectories. UDFs were written for non-built-in relations of inertial lift and magnetophoretic forces. The results were validated against our empirical data (Kumar and Rezai 2017a). Furthermore, with the validity of the model established, the unknown effects of significant parameters on MIMF such as magnetization (0–2.7 × 10^6 A/m), particle size (5–30 μm), and fluid viscosity (0.5–1.5 mPa s) were investigated in this paper. This investigation is novel both in terms of integrating the effects of multiple dominant forces on particle sorting and investigating the effect of new parameters on inertia-magnetic focusing. The presented numerical model can serve as an accessible and reliable tool to simulate inertia-magnetic phenomenon and facilitate the design of hybrid microfluidic sorting systems.

2 Numerical model

2.1 Model geometry

The schematic diagram and geometrical specifications of the modeled device were based on our experiments (Kumar and Rezai 2017a) as presented in Fig. 1. The model is a microfluidic device consisting of three regions, namely the inertia-magnetic focusing zone, the narrowing section, and the hydrodynamic expansion zone. The inertia-magnetic focusing zone was a narrow microchannel over which the magnetic particles (MPs) were affected by inertial and magnetic forces caused by the flow hydrodynamics and a permanent magnet located by the side of the channel, respectively.

Similar to our experiments (Kumar and Rezai 2017a), polystyrene paramagnetic microparticles with mean diameters of 5 and 11 μm were suspended in deionized water (DI water) with the ratio of 10:1 for 5:11 μm particles. The mixture concentration was approximately 1.1 × 10^7 particles/mL that resulted in a volumetric fraction of 0.135%. The density of particles was approximately 1.05 g/cm^3, almost the same as water density. Hence, sedimentation velocity of these particles was assumed negligible compared to their flow velocity in the forward direction. In the experiments (Kumar and Rezai 2017a), a small amount of Tween 20 (~ 0.1 wt%) was added to particle suspension to avoid any particle aggregation and to keep them dispersed in the sample. Accordingly, particle aggregation was neglected in the presented simulation. The flow rates used in our simulations were in the range of Q = 0.5–10 mL/h.

2.2 Numerical model theory

To achieve a better convergence behavior, the numerical procedure was divided into three stages. First, the steady-state solution of the flow without injecting particles or introducing the magnetic field was obtained. Then, particles were injected into the flow, where their trajectories were calculated. Finally, the magnetic field was applied to recalculate particle trajectories and achieve the final solution. The solved equations for each stage are described below.

2.2.1 Fluid flow solution

Standard laminar steady-state governing equations, i.e. the continuity Eq. (1) and the Navier–Stokes Eq. (2), without introducing the microparticles and the magnetic field, were solved for the DI water to find the converged steady-state solution of the flow:

$$\nabla \cdot \left(\rho \vec{u}\right) = 0, \tag{1}$$

$$\nabla \cdot \left(\rho \vec{u}\vec{u}\right) = -\nabla p + \nabla \cdot (\bar{\bar{\tau}}) + \rho \vec{g}. \tag{2}$$

In Eqs. (1) and (2), ρ is density, $\vec{u}$ is fluid velocity, p is static pressure, and $\bar{\bar{\tau}}$ is the stress tensor described as follows:

$$\bar{\bar{\tau}} = \mu\left[\left(\nabla\vec{u} + \nabla\vec{u}^T\right) - \frac{2}{3}\nabla \cdot \vec{u}I\right], \tag{3}$$

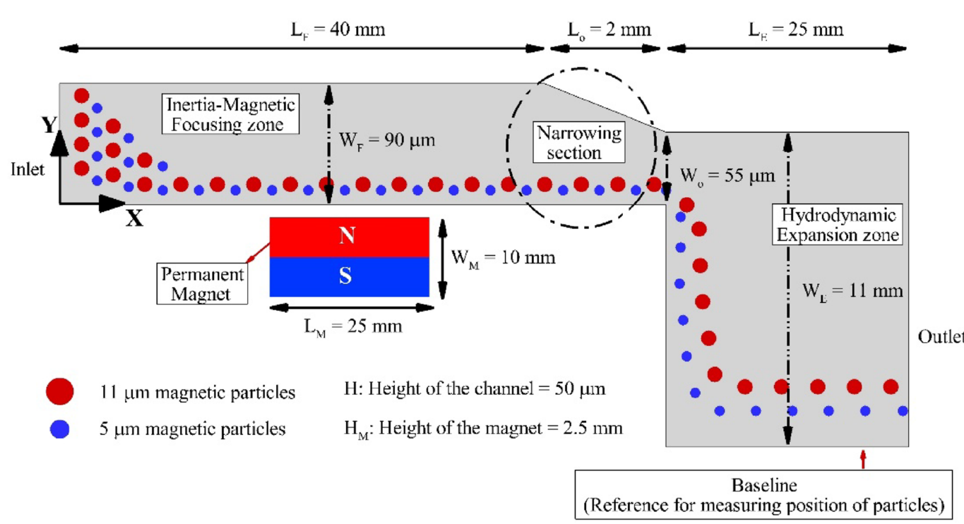

Fig. 1 Schematic diagram of the modeled MIMF microfluidic device [first introduced by Kumar and Rezai (2017a)], which consisted of an upstream inertia-magnetic focusing channel with a permanent magnet beside it, a narrowing section at the center, and a downstream hydrodynamic expansion zone and fractionation channel. The figure also shows the sizes of particles and channel sections, as well as the working principle of the device. Particle positions reported in this paper are all based on the expansion zone's bottom channel baseline

where μ is molecular viscosity, I is the identity tensor, and the second term on the right hand side is the effect of volume dilation.

2.2.2 Discrete phase modeling (DPM)

ANSYS-Fluent DPM scheme was employed to inject microparticles into the DI water and compute their trajectories in a Lagrangian reference frame. This model is used for simulating the suspensions with low particle volume fraction (< 10–12%), which is well suited for the present work with the volumetric particle fraction of 0.135%. ANSYS-Fluent predicts the trajectory of a discrete phase particle by integrating the force balance on the particle and equating it with the particle inertia in a Lagrangian reference frame as shown below (ANSYS 2018):

$$\frac{d\vec{u}_p}{dt} = F_D\left(\vec{u}_p - \vec{u}\right) + \frac{\vec{g}\left(\rho_p - \rho\right)}{\rho_p} + \vec{F}, \tag{4}$$

where $\vec{g}$ is gravitational acceleration and $\vec{F}$ is an additional acceleration term (force/unit particle mass), which accounts for the effects of inertial and magnetophoretic forces that will be added in the next stage via the use of UDFs (see next section). F_D is the drag force per unit particle mass defined by Stoke's drag law (Ounis et al. 1991):

$$F_D = 3\pi\mu d_p u_p, \tag{5}$$

where $\vec{u}_p$ is the particle velocity and d_p is the particle diameter.

The trajectory equations were solved by stepwise integration over discrete time steps. Integration of time yields the velocity of the particle at each point along the trajectory, with the trajectory itself predicted by:

$$\frac{dx}{dt} = \vec{u}_p. \tag{6}$$

2.2.3 User-defined functions (UDF)

A UDF code in C language was written and incorporated into the conventional DPM model to account for the inertial lift force (wall-induced and shear gradient-induced) and the prescribed magnetic field and the applied magnetophoretic force on the microparticles to recalculate their final trajectories. The effects of inertial lift and magnetophoretic forces acting on the particles are included in the term $\vec{F}$ of the particle force balance, Eq. (4), as shown:

$$\vec{F}_{vm} + \vec{F}_{pg} + \vec{F}_s + \vec{F} = \vec{F}_L + \vec{F}_M. \tag{7}$$

The inertial lift force ($\vec{F}_L$) has several components, (Di Carlo 2009) which include (1) rotation-induced, (2) slip-shear-induced, (3) shear gradient, and (4) wall-induced lift forces. Shear gradient and wall-induced lift forces are two dominant components of inertial force acting on a particle in a plane Poiseuille flow. Shear gradient-induced lift force pushes the particles away from the center line of the channel due to the curvature of the velocity profile. Wall-induced lift force repels the particles away from the channel walls. The magnitude of the wall-induced and shear-induced inertial lift forces on a spherical particle in a channel with square cross section are reported as follow (Martel and Toner 2014):

$$\vec{F}_{WI} = C_{WI}\frac{u_{max}^2}{D_h^4}\rho d_p^6, \tag{8}$$

$$\vec{F}_{SG} = C_{SG}\frac{u_{max}^2}{D_h}\rho d_p^3, \tag{9}$$

where C_{WI} and C_{SG} are coefficients that depends on the particle position in the channel cross section and its velocity. To account for these parameters, our simulation takes advantage of Ho and Leal general force equation that describes forces acting on small rigid spheres in low Re numbers using Lorentz generalized reciprocal theorem (Ho and Leal 1974). The resulting general force equation includes wall-induced and shear-induced lift forces, while neglecting forces originating from lag velocity or the rotation slip of the particles, as these are orders of magnitude smaller than the stresslet contribution:

$$\vec{F}_L = \frac{1}{m_p}\rho\frac{r_p^4}{D^2}\beta\left(\beta G_1(s) + \gamma G_2(s)\right)\vec{n}, \tag{10}$$

$$\beta = \left|D\left(\vec{n}\cdot\nabla\right)\vec{u}_p\right|, \tag{11}$$

$$\gamma = \left|\frac{D^2}{2}\left(\vec{n}\cdot\nabla\right)^2\vec{u}_p\right|, \tag{12}$$

$$\vec{u}_p = \left(I - \left(\vec{n}\otimes\vec{n}\right)\right)\vec{u}. \tag{13}$$

In which, $\vec{n}$ is the wall normal at the nearest point on the reference wall, ⊗ symbol represents the tensor product of the two $\vec{n}$ vectors, D is the distance between the channel walls, s is the dimensionless distance from the particle to the reference wall, and G1 and G2 are dimensionless functions of s as previously reported (Ho and Leal 1974, 1976). The inertial lift force only acts in the direction perpendicular to the velocity of the fluid. The spherical particles are further assumed to be small compared to the channel width and rotationally rigid.

The force acting on a magnetic particle due to a permanent magnet such as the one used in our experiments (Kumar and Rezai 2017a) and model in this paper can be expressed by Eq. (14) (Adams et al. 2008):

$$\vec{F}_{\mathrm{M}} = \frac{4\pi}{3} M \nabla B r_{\mathrm{p}}^{3} \frac{1}{m_{\mathrm{p}}}, \tag{14}$$

where r_p is the radius of the particle, M is magnetization and ∇B is the magnetic field gradient. Based on the data of Kumar and Rezai (2017a), magnetization and magnetic field gradient were set to 2.7×10^6 A/m and 10 T/m for validating our model, respectively. Magnetic field magnitude inside the channel was set to 300 mT. Since Eqs. (10) and (14) were not built-in expressions in the ANSYS-Fluent commercial package, a UDF code was written in C language to incorporate them into the software and investigate their effects on the final trajectories of the microparticles.

F_{vm} is the virtual mass force, the force required to accelerate the fluid surrounding the particle given by (ANSYS 2018):

$$\vec{F}_{\mathrm{vm}} = C_{\mathrm{vm}} \frac{\rho}{\rho_{\mathrm{p}}} \left(\vec{u}_{\mathrm{p}} \nabla \vec{u} - \frac{\mathrm{d}\vec{u}_{\mathrm{p}}}{\mathrm{d}t} \right), \tag{15}$$

where C_{vm} is the virtual mass factor with a value of 0.5 and ρ_p is the density of the particle. An additional force arises due to the pressure gradient in the fluid (ANSYS 2018), which is expressed as:

$$\vec{F}_{\mathrm{pg}} = \frac{\rho}{\rho_{\mathrm{p}}} \vec{u}_{\mathrm{p}} \nabla \vec{u}. \tag{16}$$

The virtual mass and pressure gradient forces can be neglected when the density of the fluid is significantly lower than that of the particles. But for our case, with particles and the fluid having relatively similar densities, these forces were included.

The Saffman's lift force, or lift due to shear, is also included in the additional force term. This lift force, $\vec{F}_s$, was adopted from Li and Ahmadi (1992), which is a generalization of the expression provided by Saffman (1965). This form of the lift force is recommended for small particle Reynolds numbers (ANSYS 2018):

$$\vec{F}_{\mathrm{s}} = \frac{2K v^{\frac{1}{2}} \rho d_{ij}}{\rho_{\mathrm{p}} d_{\mathrm{p}} \left(d_{lk} d_{kl} \right)^{\frac{1}{4}}} \left(\vec{u} - \vec{u}_{\mathrm{p}} \right), \tag{17}$$

where $K = 2.594$ and d_{ij} is the deformation tensor (ANSYS 2018).

2.2.4 Calculation procedure for the fraction of exited particles

Since ANSYS-Fluent does not directly calculate the fraction of particles exiting from the device at different regions, particle flow rate Q_p for discrete exit position ranges at the device outlet in Fig. 1 was calculated based on:

$$Q_{\mathrm{p}} = A_{\mathrm{range}} \left(\rho_{\mathrm{p,exit}} \times v_{\mathrm{p,exit}} \right). \tag{18}$$

In this equation A_{range} is the exit position range with respect to the baseline, $\rho_{p,exit}$ is the cumulative particle density of the exited particles for every range and $v_{p,exit}$ is the velocity of the exited particles. The fraction of exited particles (f) for every range was then calculated by dividing the particle flow rate of the desired range by the total particle flow rate ($Q_{p,total}$) as shown:

$$f = \frac{Q_{\mathrm{p}}}{Q_{\mathrm{p,total}}}. \tag{19}$$

2.3 Boundary conditions and solver

The boundary conditions of the microfluidic device shown in Fig. 1 were set in our model to provide the closest approximation to the experimental conditions. At the inlet section, a uniform velocity profile was imposed at the inlet in the x direction described with $u = U_{inlet}$. It should be mentioned that the longest required fully developed length for our range of flow rates ($Q = 0.5$–10 mL/h) is 0.124 mm, which is well below the channel length of 42 mm. The transverse fluid velocities in the y and z directions were both assumed to be zero ($v = w = 0$). At the outlet, a constant pressure boundary condition with zero gauge static pressure was assumed ($p_{outlet} = 0$). The non-slip boundary condition was applied on the device walls and formulated with $u = v = w = 0$.

The above equations were discretized and solved utilizing the SIMPLEC (semi implicit method for pressure linked equation consisted) algorithm. Two-way coupling was assumed between the fluid flow and the particles trajectories by which the impacts of the fluid flow on the trajectory of the particles and vice versa were considered. This is accomplished by alternately solving the discrete and continuous phase equations, until the solutions in both phases have stopped changing. Flow velocity and particle concentration were monitored as benchmark parameters to check for convergence. For all simulation cases, solutions became stabilized when residuals dropped below the prescribed value of 10^{-9}.

3 Results and discussion

We first verified our model by investigating its mesh independency and fluid flow characteristics (Sect. 3.1), then validated the model against the experimental results of Kumar and Rezai (2017a) in which a similar device was utilized (Sect. 3.2). Lastly, we used our validated model to investigate the unknown effects of magnetization (0–2.7×10^6 A/m), microparticle size (0–30 μm), and fluid viscosity (0.5–1.5 mPa s) on inertia-magnetic focusing and sorting of microparticles in a MIMF device (Sect. 3.3).

3.1 Model verification

3.1.1 Mesh independence study

The device geometry in Fig. 1 was meshed with hexahedral cells with regular connectivity (Supplementary Fig. S1). Both the narrow inertia-magnetic focusing and the expanded hydrodynamic fractionation microchannel cross sections had 45 and 25 grid points in the vertical and horizontal directions, respectively. The mesh was more refined near the microchannel walls and the entrance of the expansion zone to accurately capture the flow fluctuations around these areas.

To ensure mesh independency of our simulations, while minimizing the computational costs, several mesh sizes (i.e. number of mesh elements) in the range of 5.7×10^4 to 1.1×10^6 elements were considered. Based on our initial investigations, we found that larger flow fluctuations occur at the centerline of the inertia-magnetic focusing microchannel, especially as the flow enters the expansion zone, due to the difference between the cross section sizes. Therefore, the magnitude of axial velocity along the microchannel centerline and the axial velocity profile on the cross section of the expansion zone entrance were plotted in Fig. 2a, b, respectively, for different mesh sizes in the case of DI water flowing at 1 mL/h.

As shown in Fig. 2a, the largest velocity fluctuations along the centerline of the microchannel occur before the expansion zone, where the microchannel narrows down and the centerline velocity spikes. The axial velocity profile on the entrance cross section of the expansion zone is presented in Fig. 2b showing an expected parabolic profile. As seen in Fig. 2a, b, increasing the number of mesh elements to more than 959,125 had a negligible impact of less than 0.01% on the centerline velocity and the axial velocity profile and the flow became independent from the mesh. Therefore, this computational mesh size was chosen for our simulations.

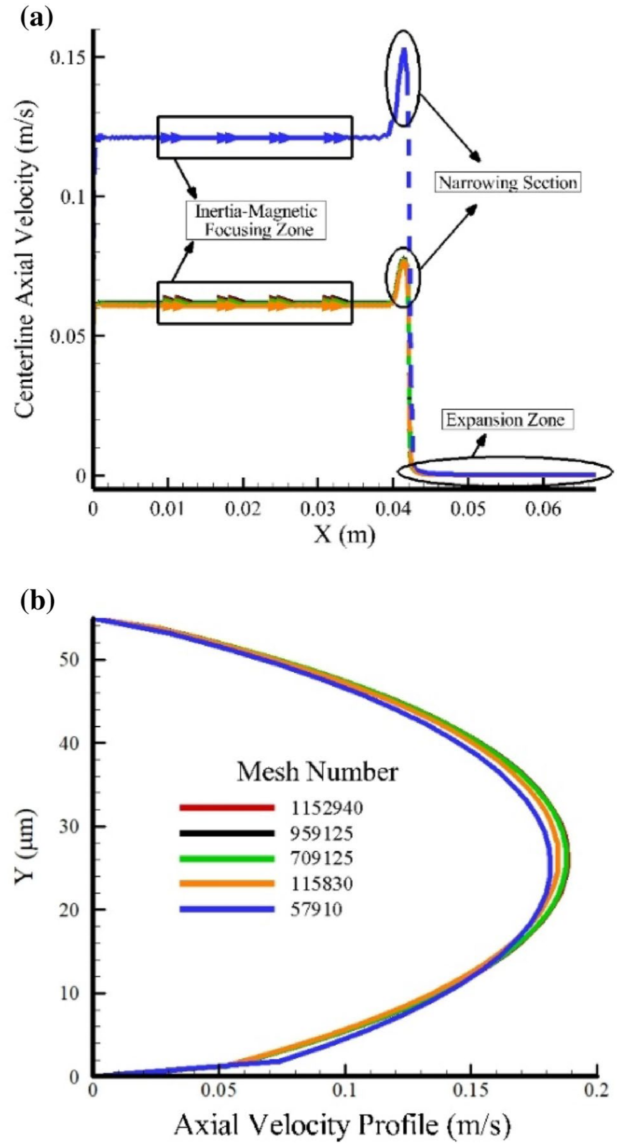

Fig. 2 Numerical simulation of DI water flowing at 1 mL/h in the MIMF device for various mesh sizes. **a** Axial velocity magnitude along the centerline of the microchannel, and **b** axial velocity profile on the entrance cross section of the expansion zone

3.1.2 Fluid flow study

We continued our verification studies by modeling the fluid velocity contours around the expansion zone entrance region without the presence of magnetic particles and the magnetic field at a flow rate of $Q = 3$ mL/h (Fig. 3). Supplementary Fig. S2 shows the flow velocity contours for different flow rates in the range of 0.5–5 mL/h.

As shown in Fig. 3 (and Supplementary Fig. S2), the flow velocity reaches a maximum local magnitude at the middle of the expansion zone entrance, due to the narrowing cross section of the microchannel just before the expansion region.

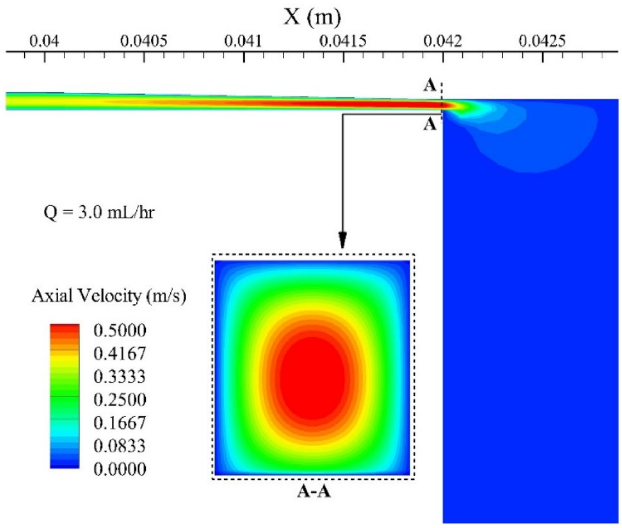

Fig. 3 Axial velocity contours at a flow rate of $Q=3$ mL/h in the MIMF device, shown around the expansion zone entrance and at its cross section

Across the cross section of the microchannel, the flow velocity is not constant, owing to the effect of viscosity. No-slip condition at the walls causes the fluid particles to become stationary, while the axial velocity increases symmetrically towards the center of the microchannel, ultimately resulting in a horseshoe-shaped parabolic velocity profile, with minimum velocity at the walls and maximum velocity at the center of the channel like a Poiseuille flow (Eyal and Quake 2002).

3.2 Model validation

After the model was verified in Sect. 3.1, we validated its performance for predicting particle trajectories against our previously published experimental results.

3.2.1 Inertial and magnetic focusing of magnetic microparticles

The capability of our model in predicting the microparticle trajectories both with and without the presence of a magnet in the MIMF device was investigated. For this, distribution of 11 µm magnetic microparticles at different flow rates was investigated around the expansion zone of the device and compared to the results of Kumar and Rezai (2017a) in Fig. 4.

For all the flow rates, 11 µm magnetic microparticles were found to be randomly distributed in the channel without the magnetic field in our model (Fig. 4a). However, when we introduced the magnetic field (Fig. 4b), microparticles were found to be magnetically focused at the side channel of the focusing region and deflected as a narrow particle band into the expansion region. These results match perfectly with the experimental results of Kumar and Rezai in Fig. 4c (Kumar and Rezai 2017a). Moreover, as shown in Fig. 4a with no magnetic focusing, microparticles focus weakly in the expansion region as the flow rate was increased from 1 to 5 mL/h. This observation, which is experimentally supported (Fig. 4c), can be attributed to the inertial forces acting on the magnetic microparticles that are more pronounced at higher flow rates (Mach and Di Carlo 2010; Martel and Toner 2014; Shardt et al. 2012).

3.2.2 Effect of magnetic focusing on the exit position of microparticles

Further model validation attempts were made quantitatively by investigating the exit position of magnetic microparticles with and without modeling the magnetic focusing effect. The fraction of particles (f) was calculated at the exit region of the MIMF device, with respect to the bottom sidewall of the expansion channel (i.e. baseline in Fig. 1), for the 11 µm magnetic microparticles flowing at 3 mL/h. Results were compared with the experimental data (Kumar and Rezai 2017a) in Fig. 5.

As shown experimentally (Kumar and Rezai 2017a) in Fig. 5, without magnetic focusing, the particles were randomly dispersed along a wide range of the outlet, 3.5–8.4 mm away from the sidewall. However, magnetically focused particles fell within a narrower range of the outlet concentrating at 2.0–2.4 mm from the sidewall. Numerical simulations predicted the exit position of microparticles to be 1.98–2.42 mm and 3.42–8.33 mm from the sidewall, for the cases with and without magnetic focusing, respectively. The numerical simulation for both cases found particles to be distributed approximately 0.05 mm wider than the experiments. The discrepancy between the numerical simulation and the experiments was greater for the fraction of particles, especially for the case without magnetic focusing in the mid-range of 5.25–5.95 mm. Maximum discrepancy was found to be around 10% within the range of 5.25–5.6 mm.

3.2.3 Effect of flow rate on inertia-magnetic focusing of microparticles

We also investigated the effect of flow rate on the exit position of 11 µm magnetic microparticles at the device outlet and validated our numerical simulation with the experimental measurements (Kumar and Rezai 2017a). Particles' exit position flowing at different flow rates in the presence of magnetic field is displayed along the outlet in Fig. 6 for both the present simulation and the experimental cases.

As shown in Fig. 6, the particles were deflected further away from the channel sidewall with increasing the flow rate. The focusing zone ranges in the simulations were

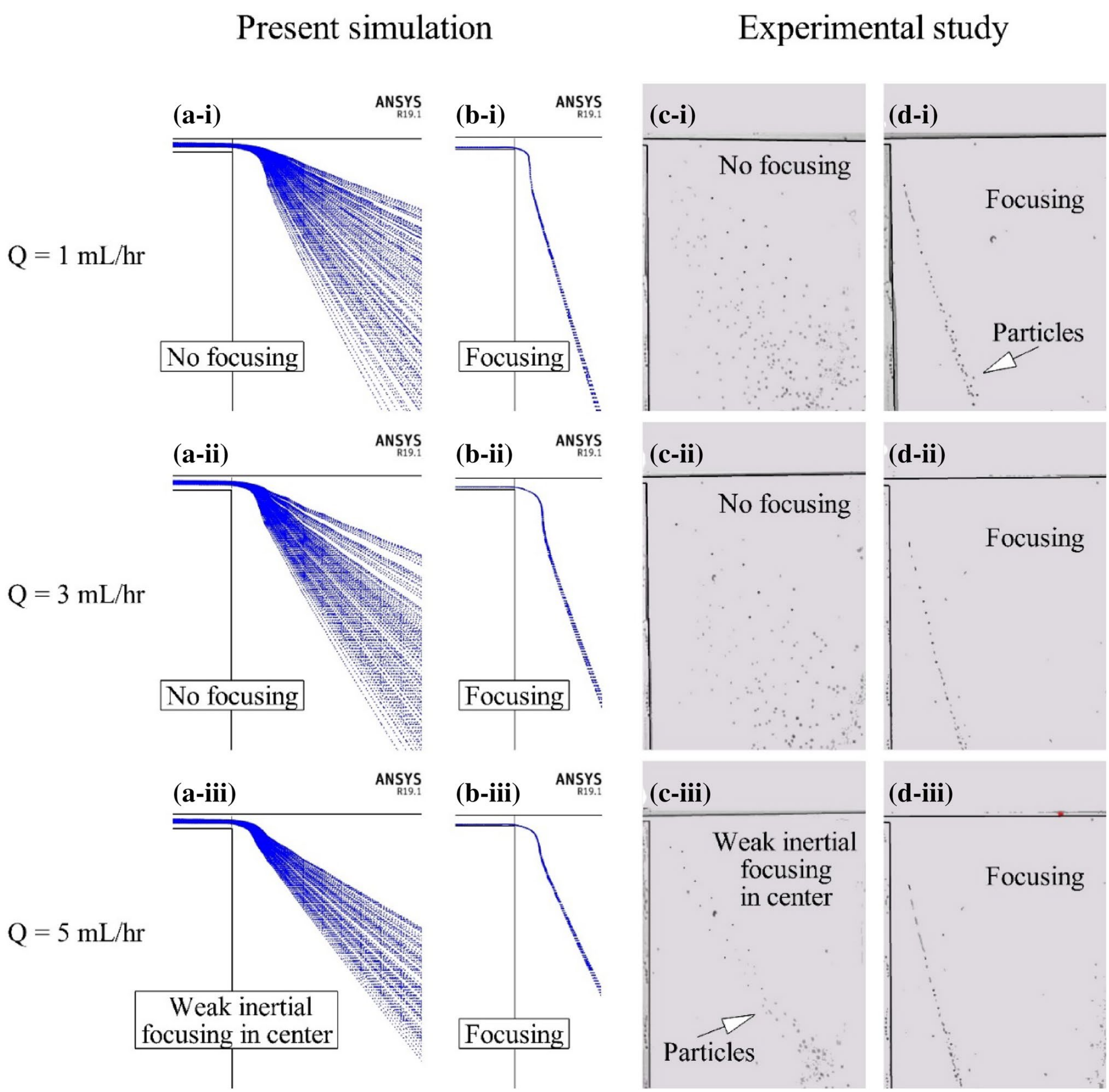

Fig. 4 Distribution of 11 µm magnetic microparticles at different flow rates around the expansion zone of the MIMF device, for the cases of numerical simulation **a** without and **b** with magnetic focusing, as well as experimental results **c** without and **d** with magnetic focusing. Experimental figures were reproduced based on the work of Kumar and Rezai (2017a), with the permission from Springer Nature

1.72–1.98, 1.98–2.11, and 2.29–2.46 mm for the flow rates of 0.5, 1, and 5 mL/h, respectively. In experiments (Kumar and Rezai 2017a), these ranges were 1.73–1.97, 1.92–2.22, and 2.27–2.47 mm for 0.5, 1, and 5 mL/h flow rates, respectively. These findings indicate that the numerically predicted exit positions of the particles correspond well with the experimental data (Kumar and Rezai 2017a) with a mismatch of less than 5%. This increase in particle deflection with increase in the flow rate can be attributed to the inertial lift force acting against the magnetic force. For particle Reynolds number, Re_p, larger than one, inertial lift force becomes more important and microfluidic inertial focusing is being realized (Mach and Di Carlo 2010; Martel and Toner 2014). In our case, for the flow rate of 5 mL/h ($Re_{p,11} = 1.12$), inertial force becomes significant, but not enough to dominate the magnetic focusing at the

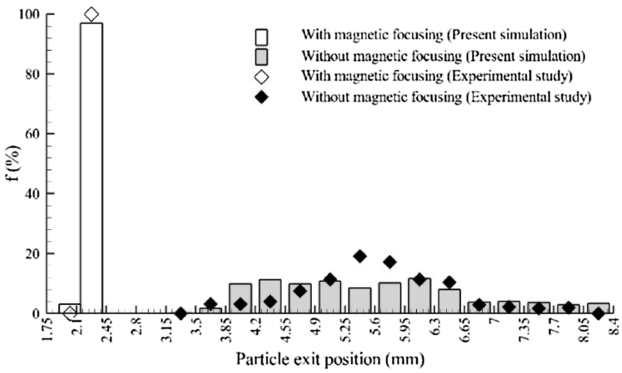

Fig. 5 Comparison of the experimental (Kumar and Rezai 2017a) and numerical exit positions (at the device outlet) of 11 µm magnetic microparticles flowing at 3 mL/h in the MIMF device

sidewall. The particles were still mainly pulled toward the sidewall at this flow rate, while being deflected approximately 5% of the width of the expansion zone toward the channel center.

3.2.4 Duplex inertia-magnetic fractionation of microparticles

For final step of model validation, inertia-magnetic sorting of two microparticles with different sizes was investigated. These numerical results are compared against the experimental measurements for the mixture of 5 µm and 11 µm magnetic microparticles flowing at 5 mL/h in the channel as shown in Fig. 8.

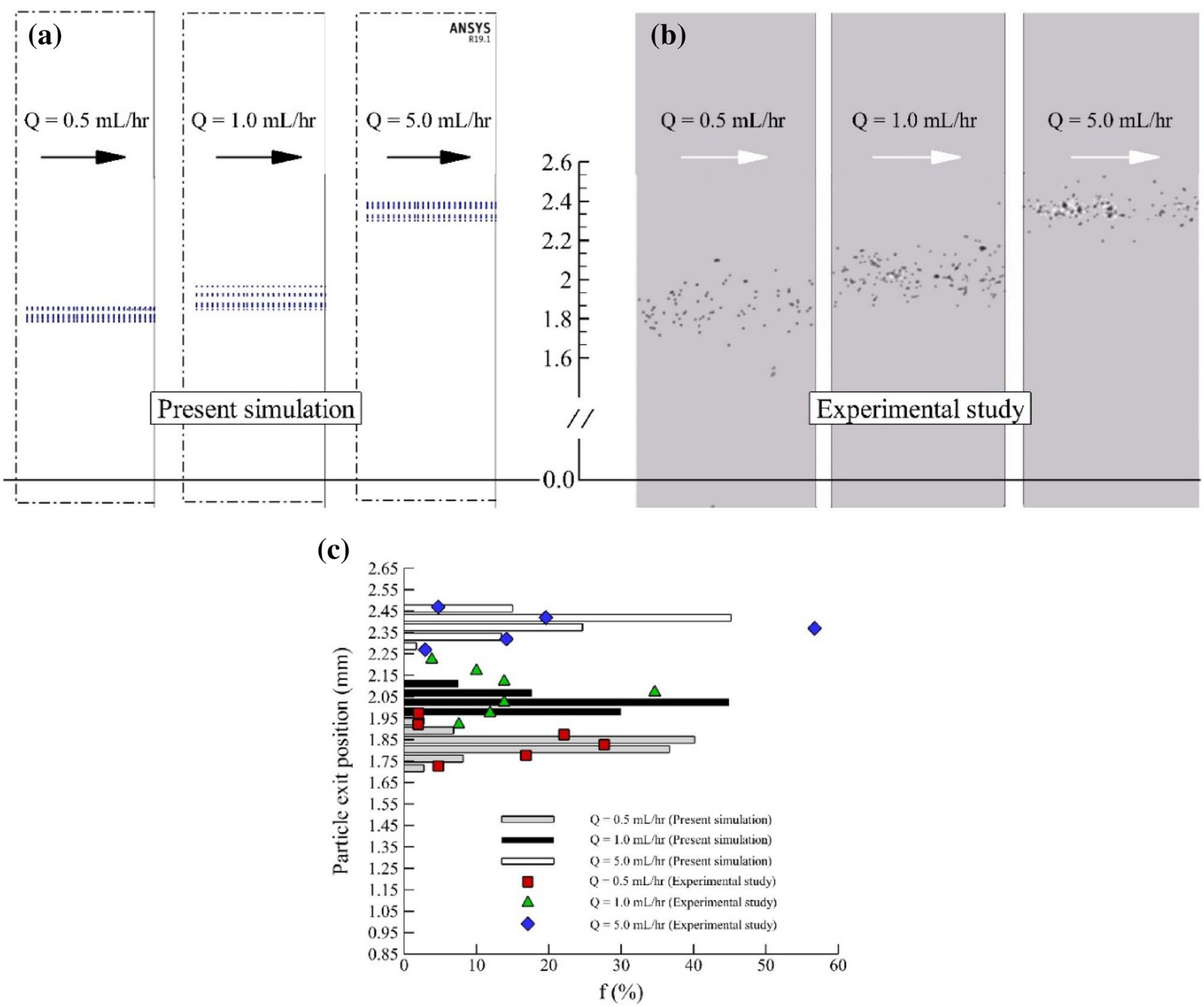

Fig. 6 Effect of flow rate on exit position of magnetically focused 11 µm microparticles in the MIMF device. **a** Present simulation. **b** Experimental study (Kumar and Rezai 2017a) with permission from Springer Nature. **c** Exit position of magnetically focused 11 µm particles demonstrating both the numerical and experimental results

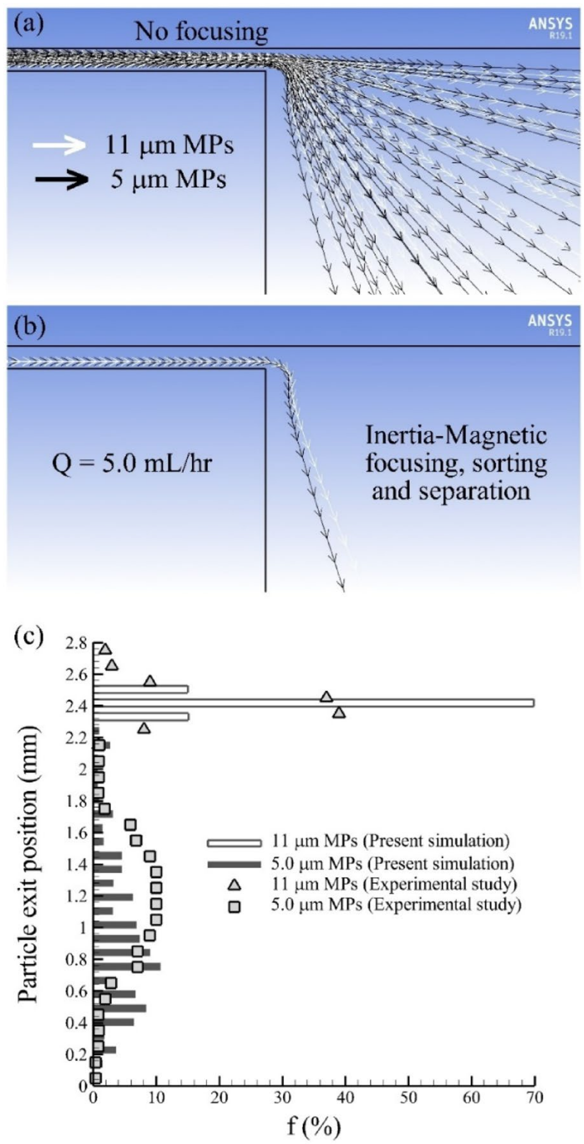

Fig. 7 Distribution of 5 and 11 μm magnetic particles flowing at 5 mL/h in the MIMF device considering the effects of inertia-magnetic sorting for the cases of **a** without the magnet and **b** with the magnet at the entrance to the expansion region. **c** Magnetically focused particles exit positions at the outlet of the MIMF device featuring both the numerical and experimental results

As shown in Fig. 7a, without introducing the magnetophoretic force, microparticles of both sizes enter the expansion zone region completely unsorted and randomly distributed throughout a wide range of the channel. In contrast, when we repeated the simulation under the same condition except with introducing the magnetic field (Fig. 7b), we observed the streams of magnetically focused microparticles to be separated based on their difference in size. The spatial fraction distribution of particles at the outlet is shown in Fig. 7c. It was found that 5 μm and 11 μm particles were distributed within the range of 0.10–2.20 mm and 2.29–2.46 mm, respectively, while in the experiments (Kumar and Rezai 2017a), this range was found to be 0.05–2.15 mm (for 5 μm) and 2.15–2.75 mm (for 11 μm). Despite imposing the same throughput at the inlet as that of the experiment, to assess if the same amount of particles exits the domain after the simulation, we recalculated the rate of particles per second at the outlet to report the possible inconsistencies due to particles loss or accumulation in the domain. The simulation results predicted a fractionation efficiency and particle throughput of 100% and 1.38×10^4 particles/s at the outlet, respectively, while these parameters were reported to be 98% and 1.3×10^4 particles/s in the experiments (Kumar and Rezai 2017a). Again, an acceptable agreement is observed with the errors of 2% and 6% for the fractionation efficiency and throughput, respectively.

3.3 Parametric numerical studies

3.3.1 Further investigation of duplex inertia-magnetic fractionation

Initially, we analyzed cross-sectional particle trajectories along the channel length for two flow rates in Fig. 8.

As shown in Fig. 8a, particles are randomly injected into the domain and move along the length of the channel. At 10 mL/h (Fig. 8a-ii), soon after injection, particles start to migrate away from the sidewalls to the center of the channel as inertial lift forces are more dominant at this flow rate. As expected, particle trajectories are deflected toward the bottom side of the channel as soon as they enter the magnetic zone (Fig. 8b). But this deflection is different for different flow rates and particle sizes. Based on Fig. 8b, 11 μm particles are quicker to migrate to the bottom side of the channel compared with the 5 μm ones. Also at 1 mL/h (Fig. 8b–i), particles' migration to the bottom side is quicker than the 10 mL/h, as the inertial lift and the drag forces which depend on particle velocity are less pronounced at lower flow rates to resist the magnetophoretic force. At the magnetic zone exit (Fig. 8c), particles are fully focused at the bottom side of the channel, while at 10 mL/h, 11 μm particles focus at two inertial equilibrium positions at 22 μm away from the centerline of the channel.

As hypothesized by Kumar and Rezai (2017a), by increasing the flow rate, the effect of inertial force becomes more dominant on large particles (also shown in Fig. 8c). Moreover, because of the 3D paraboloid nature of the velocity profile in a rectangular cross section, it was claimed that the 11 μm magnetic particles would follow symmetric streamlines, while the 5 μm magnetic particles would lie on various ones in the experiments conducted in Sect. 3.2.4. Consequently, 5 μm magnetic particles become distributed over a larger region compared to 11 μm magnetic particles as shown in Fig. 7c (Kumar and Rezai 2017a). To investigate

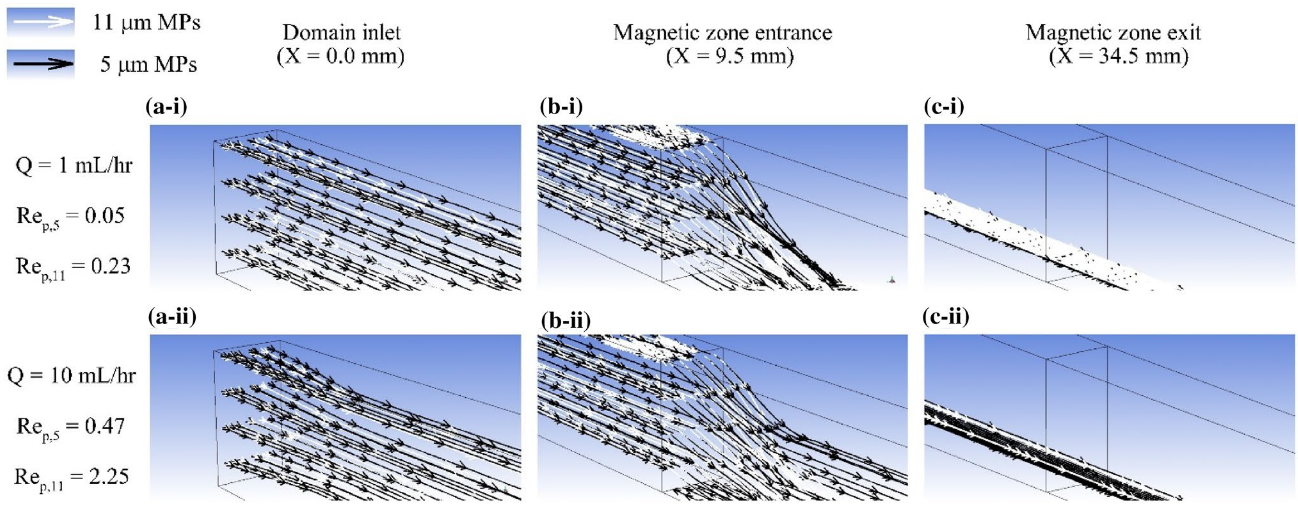

Fig. 8 Particle trajectories of 5 μm and 11 μm magnetic microparticles flowing at different flow rates near the **a** domain inlet, **b** magnetic zone entrance, and **c** magnetic zone exit

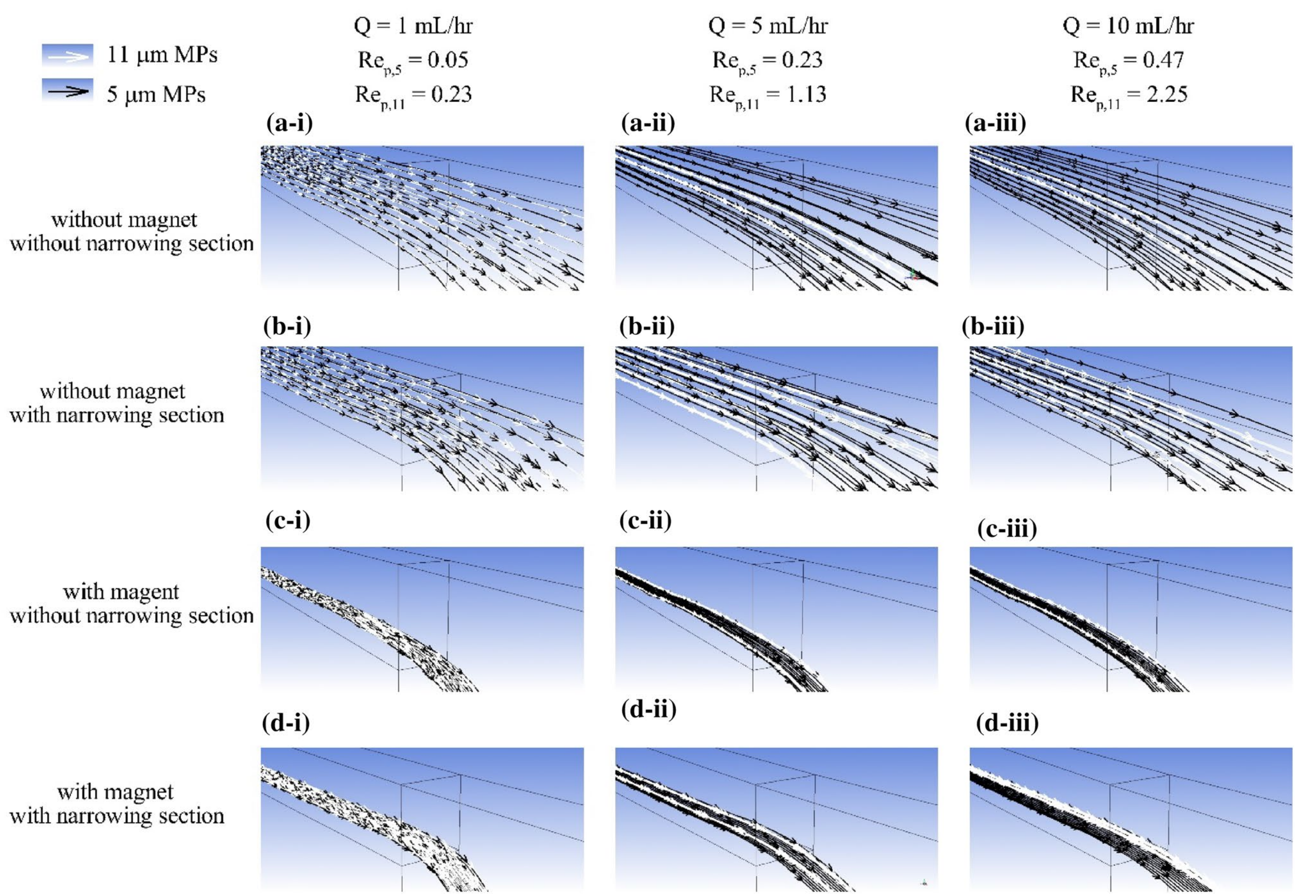

Fig. 9 Distribution of 5 μm and 11 μm magnetic microparticles flowing at different flow rates near the expansion zone entrance of the MIMF device, for the cases of **a** without magnet and narrowing section, **b** without magnet and with narrowing section, **c** with magnet and without narrowing section, and **d** with magnet and narrowing section

the potentially significant effect of inertial lift and study its impact on focusing and separation of particles, we simulated the 3D distribution of 5 µm and 11 µm particles at different flow rates around the expansion zone entrance of the device (Fig. 9), considering the effects of the magnet and the narrowing section right before the expansion region (shown by $L_o = 2$ mm and $W_o = 55$ µm in Fig. 1). For better visibility, please refer to Supplementary Fig. S3, which only shows the 3D distribution of 11 µm particles in the channel.

Microparticles flowing in rectangular microchannels migrate to two equilibrium positions along the larger side of the channel due to the shear and wall-induced lift forces (Di Carlo 2009; Di Carlo et al. 2007; Zhou and Papautsky 2013), provided that the particle Reynolds number exceeds unity. As shown in Fig. 9a–d, for all the studied flow rates of 1–10 mL/h, 5 µm particles have particle Reynolds numbers lower than 1 ($0.05 \leq Re_{p,5} \leq 0.47$). Expectedly, no significant inertial focusing is observed for these particles in any of the investigated cases. Without the magnet (Fig. 9a, b), 5 µm particles are dispersed throughout the channel, while adding the magnet (Fig. 9c, d) results in their magnetic focusing on a plane against the channel wall close to the external magnet. This multi-streamline focusing explains why 5 µm particles were found to be distributed over a wider range of the outlet in both simulation and experimental data in Fig. 9c, proving Kumar and Rezai's hypothesis to be correct (Kumar and Rezai 2017a).

For 11 µm particles, Reynolds number exceeds unity and becomes $Re_{p,11} = 1.13$ and $Re_{p,11} = 2.25$ at 5 mL/h and 10 mL/h flow rates, respectively. In Fig. 9a, without both the magnet and the narrowing section in the setup, 11 µm particles were focused at the center of the two largest sides and approximately 20 µm and 22 µm away from the centerline of the channel at 5 mL/h and 10 mL/h flow rates, respectively (see Fig. S3 for clearer view). When we added the narrowing section in the setup in Fig. 9b, making the end cross section almost square shape, we observed particles migrating to all four sides of the square cross section, but not fully focus at their center points. This can be explained by the short length of the narrowing section ($L_o = 2$ mm) that might not allow for full focusing considering the low particle Reynolds numbers. With introducing the magnetophoretic force in the setup in Fig. 9c, particles moved to the bottom side of the channel, while 11 µm particles still remained inertially focused at two equilibrium positions and approximately 20 µm and 22 µm away from the centerline of the channel at 5 mL/h and 10 mL/h flow rates, respectively. Adding the narrowing section at the end (Fig. 9d) caused the 11 µm particles to move away from the sidewalls and focus more at the center of the channel, especially for the higher flow rate of 10 mL/h. In this case, 11 µm particles focused at 15 µm and 9 µm away from the centerline of the square shape cross section at 5 mL/h and 10 mL/h flow rates, respectively.

Furthermore, comparing particle trajectories at two different locations of magnetic zone exit (Fig. 8c-i, c-ii) and expansion zone entrance (Fig. 9c-i, d-i, c-iii, d-iii), a slight deflection of particles away from the bottom side toward the center of the channel is noticeable at the expansion zone entrance, especially for higher flow rate of 10 mL/h. This can be attributed to the removal of the magnetophoretic force in the section following the magnetic zone exit until the expansion zone entrance ($34.5 \text{ mm} < X < 42$ mm) that leaves the inertial lift and the drag as dominant forces determining the particles equilibrium positions. Numerical results show that at 10 mL/h, particles equilibrium positions are approximately 5 µm higher at the expansion zone entrance than the magnetic zone exit.

3.3.2 Effect of magnetization on inertia-magnetic focusing of microparticles

With the numerical model validated against the experimental measurements, we investigated the effect of other important parameters on the focusing of microparticles, starting with the magnetization effect, *M*. Magnetization can be changed using different magnets and their orientation and positioning in the MIMF device to enhance the quality and efficiency of particle focusing and sorting. Accordingly, we investigated the exit position of 11 µm magnetic particles flowing at 3 mL/h in the MIMF device with different magnetizations in Fig. 10.

As displayed in Fig. 10, by increasing the magnetization, particles' focusing quality was enhanced significantly. With no magnet in the setup, particles were randomly distributed over a wide region of the outlet within 3.42–8.33 mm from the baseline. Increasing the magnetization to 4.5×10^5 A/M (~ 17% of the experimental value (Kumar and Rezai 2017a)) enhanced the effect of magnetic focusing. In this case, particles were found to be distributed over a narrower range of 2.42–3.82 mm from the baseline. For magnetizations higher than 1.35×10^6 A/M [~ 50% of the experimental value (Kumar and Rezai 2017a)], magnetic saturation was achieved and no significant change in the focusing was observed. For these cases, particle distribution ranges were found to be almost identical to those of the experiment at 2.02–2.46 mm. This study indicates that some design modifications can be considered to accommodate even a weaker magnet, with the same length, in this microfluidic setup to achieve similar results. At lower magnetization values of 4.5×10^5 A/m, increasing the length of the magnet may also allow the particles to better focus along the channel sidewall before entering the expansion zone.

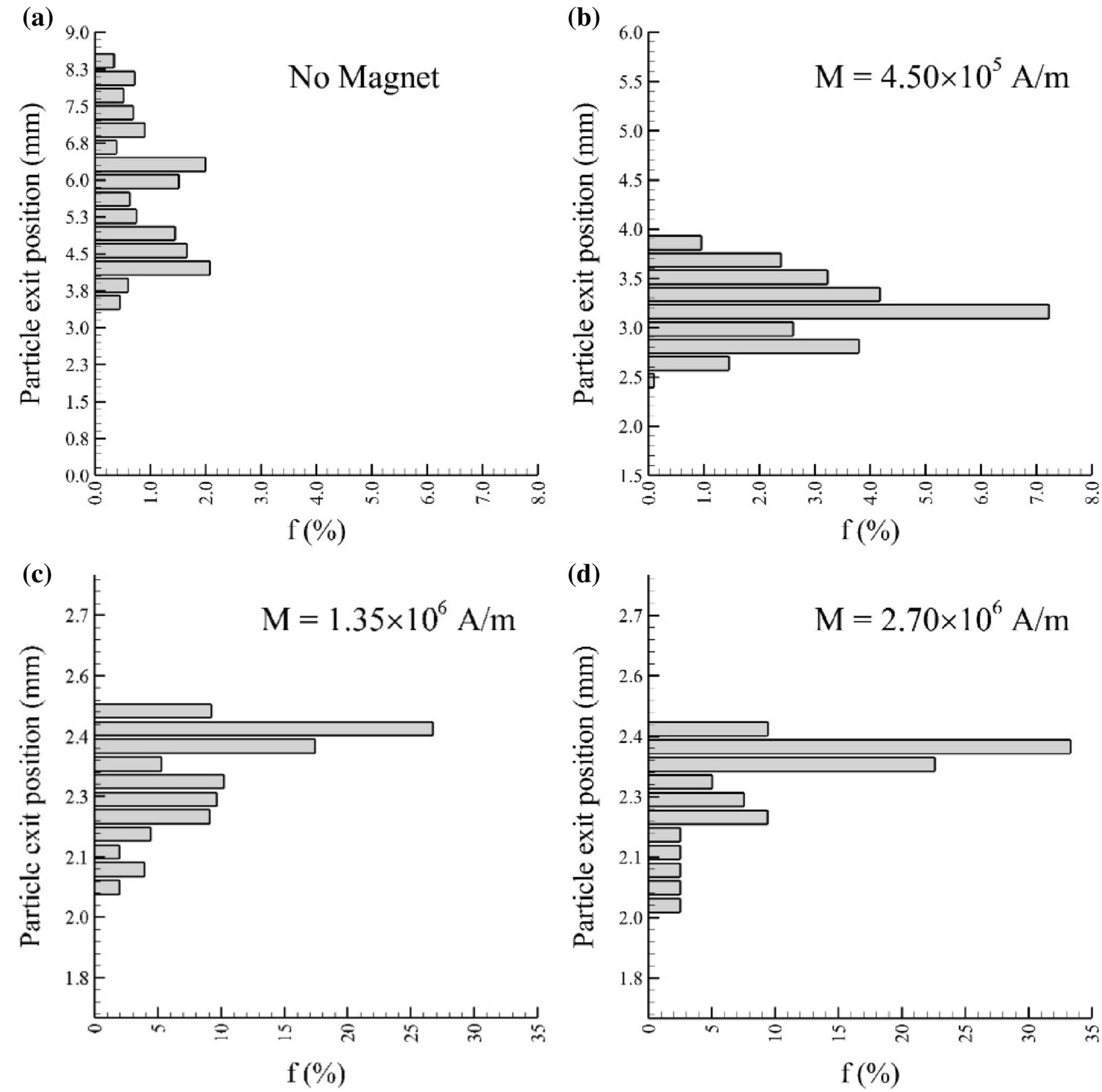

Fig. 10 Exit position of magnetically focused 11 μm particles flowing at 3 mL/h with different magnetization magnitudes of **a** no magnet, **b** 4.50×10^5 A/m, **c** $M=1.35\times10^6$ A/m, and **d** $M=2.7\times10^6$ A/m

3.3.3 Effect of microparticle diameter on inertia-magnetic focusing

Microparticles of various sizes are used as surrogates for biological substances to design microfluidic sorters or as carriers for conjugation of target analytes and their separation. The impact of changing the microparticle size on their inertia-magnetic focusing and exit position from the MIMF device was also studied numerically. The distribution of magnetic microparticles with different diameters of 5, 11, 20, and 30 μm, flowing at 0.5 mL/h is displayed in Fig. 11. Magnetization was kept at 2.7×10^6 A/M in all cases, similar to the previously used experimental value.

The exit positions were found to be 1.54–1.72 mm, 1.72–1.89 mm, 1.94–2.11 mm, and 2.20–2.33 mm for 5, 11, 20, and 30 μm microparticles, respectively. As demonstrated, there is a direct relation between the particles exit position and their size, meaning that larger particles concentrate

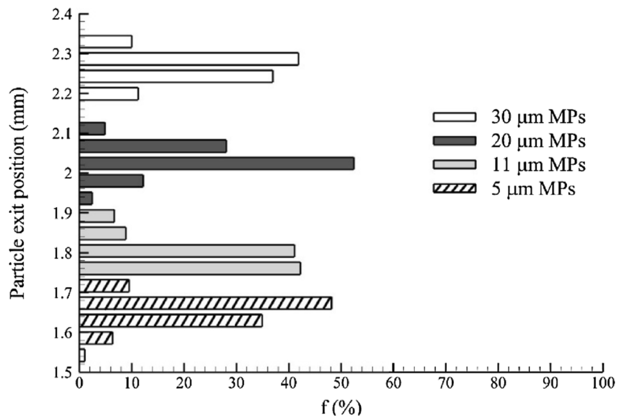

Fig. 11 Exit position of inertia-magnetically focused microparticles with different sizes flowing at 0.5 mL/h in the MIMF device. Magnetization was 2.7×10^6 A/M in all cases

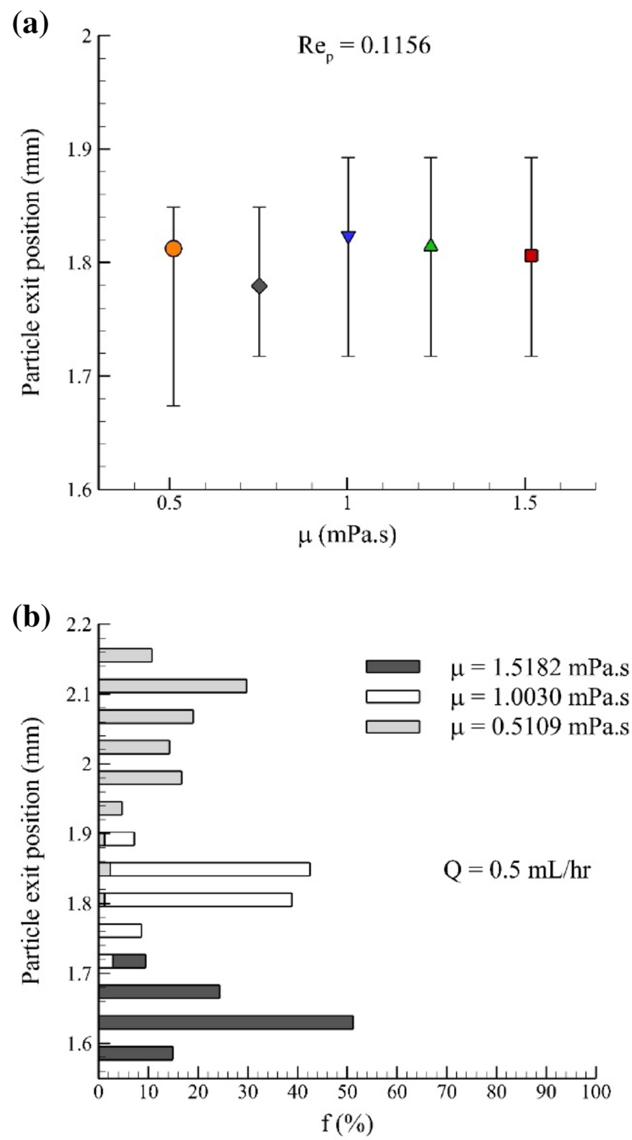

Fig. 12 Effect of fluid viscosity on exit position of inertia-magnetically focused 11 μm particles at **a** $Re_p = 0.1156$ and **b** Q = 0.5 mL/h. Magnetization was 2.7×10^6 A/M in all cases

further away from the baseline at a given flow rate. After inertia-magnetic focusing on top of the magnet, larger particles experience larger inertial forces toward the center of the channel in the narrowing section, hence they assume positions further away from the baseline. This modeling also demonstrated that a fourplex separation is achievable for the range of particles, magnetization and flow rate reported above. This was later shown in almost similar settings by Kumar and Rezai (2017b).

3.3.4 Effect of fluid viscosity on inertia-magnetic focusing of microparticles

Recently, a significant attention has been given to fluids other than water due to the prominence of viscoelastic and non-Newtonian solutions in various biomedical applications (Lu et al. 2017; Nam et al. 2012, 2015; Zhang et al. 2016; Zhou et al. 2019). Hence, we became interested in studying the effect of fluid viscosity on inertia-magnetic focusing of microparticles in the MIMF device. DI water properties were obtained from Sabaghan et al. (2016) with the density being relatively unchanged within the studied temperature range of 5 °C ≤ T ≤ 55 °C. The results are presented for 11 μm particles in two cases of constant Re_p and constant flow rate in Fig. 12a, b, respectively. Magnetization was kept at 2.7 × 106 A/M in all cases.

As shown in Fig. 12a, for the case of constant particle Reynolds number, changes in fluid viscosity barely had an impact on the particle exit position. The 11 μm particles exited the device within the range of 1.67–1.89 mm with a mean position of 1.81 mm, when fluid viscosity was decreased from 1.52 to 0.51 mPa s. Drag force on the particles is directly dependent on the fluid dynamic viscosity and particle velocity (see Eq. 5). To keep the particle Reynolds number (Re_p) constant, we needed to increase the flow rate as well to compensate for the increased viscosity. Therefore, drag force and the resulting hydrodynamic separation would not change significantly. On the other hand, at a constant flow rate of 0.5 mL/h in Fig. 12b, as the fluid viscosity declined (Re_p increased), particles were focused further away from the baseline. In this case, the exit position of 11 μm particles was 1.59–1.72, 1.63–1.85, 1.72–1.89, 1.76–1.94, and 1.80–2.16 mm for the fluid viscosities of 1.52, 1.23, 1.00, 0.75, and 0.51 mPa s, respectively (some are not shown in Fig. 12b due to overlap and for better visualization of other data points). At a constant flow rate and particle diameter (Fig. 12b), increasing the viscosity increases the drag force on the particles, while not changing other acting forces significantly (Eqs. 5–14). In the narrowing section, particles experience larger drag forces toward the channel sidewall in more viscous fluids; hence, they assume positions closer to the baseline.

4 Conclusion

In this study, a numerical approach was established to simulate our MIMF method for microfluidic-based particle sorting (Kumar and Rezai 2017a). UDF codes were developed to account for the combined effects of magnetophoretic and inertial lift forces that are not built-in relations in ANSYS-Fluent. Magnetic focusing of microparticles was investigated by utilizing 11 µm particles at various flow rates (0.5–5 mL/h). Then, inertia-magnetic sorting of microparticles was studied by flowing a mixture of 5 µm and 11 µm particles at 5 mL/h. The presented model is able to successfully predict particle trajectories for both cases of randomly distributed and magnetically focused microparticles. The simulation results were validated against experimental measurements (Kumar and Rezai 2017a). The fractionation efficiency and throughput of the method were predicted to be 100% and 1.38×10^4 particles/s, respectively. Inertial focusing of magnetic particles was also investigated, considering the impact of rectangular and square-shaped cross sections. Finally, a parametric study was performed to study the impact of significant parameters such as magnetization, particle size, and fluid properties on magnetic focusing and MIMF. The presented numerical model can be used as a reliable tool to simulate sorting of particles and biological cells based on their sizes and magnetic characteristics. In conjunction with experimental studies, it can potentially lead to a better understanding of this phenomenon and a more optimized design of the microfluidic-based sorting systems.

Acknowledgements This research has received funding support from Kuwait Foundation for the Advancement of Sciences under project code: PN18-15EC-04 (PR, AE) and Ontario Ministry of Agriculture, Food and Rural Affairs (PR). Such support does not indicate endorsement by Kuwait Foundation for the Advancement of Sciences or the Government of Ontario of the contents of this material.

Compliance with ethical standards

Conflict of interest There are no conflicts to declare.

References

Adams JD, Kim U, Soh HT (2008) Multitarget magnetic activated cell sorter. Proc Natl Acad Sci USA 105:18165–18170. https://doi.org/10.1073/pnas.0809795105

Amin A (2014) High throughput particle separation using differential fermat spiral microchannel with variable channel width. University of Akron, Akron

Andersson H, Van den Berg A (2003) Microfluidic devices for cellomics: a review Sensors and actuators B. Chemical 92:315–325

ANSYS I (2018) ANSYS Fluent Theory Guide 19.0

Applegate RW Jr et al (2006) Microfluidic sorting system based on optical waveguide integration and diode laser bar trapping. Lab Chip 6:422–426

Baker CA, Duong CT, Grimley A, Roper MG (2009) Recent advances in microfluidic detection systems. Bioanalysis 1:967–975

Bayat P, Rezai P (2018) Microfluidic curved-channel centrifuge for solution exchange of target microparticles and their simultaneous separation from bacteria. Soft Matter 14:5356–5363

Bélanger MC, Marois Y (2001) Hemocompatibility, biocompatibility, inflammatory and in vivo studies of primary reference materials low-density polyethylene and polydimethylsiloxane: a review. J Biomed Mater Res 58:467–477

Bhagat AAS, Kuntaegowdanahalli SS, Papautsky I (2008) Continuous particle separation in spiral microchannels using dean flows and differential migration. Lab Chip 8:1906–1914

Chalmers JJ, Zborowski M, Sun L, Moore L (1998) Flow through, immunomagnetic cell separation. Biotechnol Progress 14:141–148

Chen J, Li J, Sun Y (2012) Microfluidic approaches for cancer cell detection, characterization, and separation. Lab Chip 12:1753–1767

Cheng C, Yang L, Zhong M, Deng W, Tan Y, Xie Q, Yao S (2018) Au nanocluster-embedded chitosan nanocapsules as labels for the ultrasensitive fluorescence immunoassay of *Escherichia coli* O157:H7. Analyst 143:4067–4073. https://doi.org/10.1039/c8an00987b

Dalili A, Samiei E, Hoorfar M (2019) A review of sorting, separation and isolation of cells and microbeads for biomedical applications: microfluidic approaches. Analyst 144:87–113. https://doi.org/10.1039/c8an01061g

Di Carlo D (2009) Inertial microfluidics. Lab Chip 9:3038–3046

Di Carlo D, Irimia D, Tompkins RG, Toner M (2007) Continuous inertial focusing, ordering, and separation of particles in microchannels. Proc Natl Acad Sci 104:18892–18897

Eyal S, Quake SR (2002) Velocity-independent microfluidic flow cytometry. Electrophoresis 23:2653–2657

Feng J, Hu HH, Joseph DD (1994a) Direct simulation of initial value problems for the motion of solid bodies in a Newtonian fluid Part 1. Sedimentation. J Fluid Mech 261:95–134

Feng J, Hu HH, Joseph DD (1994b) Direct simulation of initial value problems for the motion of solid bodies in a Newtonian fluid. Part 2. Couette and Poiseuille flows. J Fluid Mech 277:271–301

Forbes TP, Forry SP (2012) Microfluidic magnetophoretic separations of immunomagnetically labeled rare mammalian cells. Lab Chip 12:1471–1479

Geens M, Van de Velde H, De Block G, Goossens E, Van Steirteghem A, Tournaye H (2006) The efficiency of magnetic-activated cell sorting and fluorescence-activated cell sorting in the decontamination of testicular cell suspensions in cancer patients. Hum Reprod 22:733–742

Hale C, Darabi J (2014) Magnetophoretic-based microfluidic device for DNA isolation. Biomicrofluidics 8:044118

Hejazian M, Li W, Nguyen N-T (2015) Lab on a chip for continuous-flow magnetic cell separation. Lab Chip 15:959–970

Ho B, Leal L (1974) Inertial migration of rigid spheres in two-dimensional unidirectional flows. J Fluid Mech 65:365–400

Ho B, Leal L (1976) Migration of rigid spheres in a two-dimensional unidirectional shear flow of a second-order fluid. J Fluid Mech 76:783–799

Hoffmann C, Franzreb M, Holl W (2002) A novel high-gradient magnetic separator (HGMS) design for biotech applications. IEEE Trans Appl Supercond 12:963–966

Huang LR, Cox EC, Austin RH, Sturm JC (2004) Continuous particle separation through deterministic lateral displacement. Science 304:987–990

Jiang Y, Zou S, Cao X (2016) Rapid and ultra-sensitive detection of foodborne pathogens by using miniaturized microfluidic devices: a review. Anal Methods 8:6668–6681. https://doi.org/10.1039/C6AY01512C

Julius M, Masuda T, Herzenberg L (1972) Demonstration that antigen-binding cells are precursors of antibody-producing cells after purification with a fluorescence-activated cell sorter. Proc Natl Acad Sci 69:1934–1938

Karabacak NM et al (2014) Microfluidic, marker-free isolation of circulating tumor cells from blood samples. Nat Protoc 9:694

Kim MJ, Lee DJ, Youn JR, Song YS (2016) Two step label free particle separation in a microfluidic system using elasto-inertial focusing and magnetophoresis. RSC Adv 6:32090–32097. https://doi.org/10.1039/C6RA03146C

Krishnan JN, Kim C, Park HJ, Kang JY, Kim TS, Kim SK (2009) Rapid microfluidic separation of magnetic beads through dielectrophoresis and magnetophoresis. Electrophoresis 30:1457–1463

Kumar V, Rezai P (2017a) Magneto-Hydrodynamic Fractionation (MHF) for continuous and sheathless sorting of high-concentration paramagnetic microparticles. Biomed Microdevices 19:39

Kumar V, Rezai P (2017b) Multiplex Inertio-Magnetic Fractionation (MIMF) of magnetic and non-magnetic microparticles in a microfluidic device. Microfluid Nanofluid 21:83

Lee MG, Shin JH, Bae CY, Choi S, Park J-K (2013) Label-free cancer cell separation from human whole blood using inertial microfluidics at low shear stress. Anal Chem 85:6213–6218

Li A, Ahmadi G (1992) Dispersion and deposition of spherical particles from point sources in a turbulent channel flow. Aerosol Sci Technol 16:209–226

Li P et al (2015) Acoustic separation of circulating tumor cells. Proc Natl Acad Sci 112:4970–4975

Lu X, Liu C, Hu G, Xuan X (2017) Particle manipulations in non-Newtonian microfluidics: a review. J Colloid Interface Sci 500:182–201

Mach AJ, Di Carlo D (2010) Continuous scalable blood filtration device using inertial microfluidics. Biotechnol Bioeng 107:302–311

Martel JM, Toner M (2014) Inertial focusing in microfluidics. Annu Rev Biomed Eng 16:371–396

Matas J-P, Morris JF, Guazzelli É (2004) Inertial migration of rigid spherical particles in Poiseuille flow. J Fluid Mech 515:171–195

Modak N, Datta A, Ganguly R (2009) Cell separation in a microfluidic channel using magnetic microspheres. Microfluid Nanofluid 6:647

Modak N, Kejriwal D, Nandy K, Datta A, Ganguly R (2010) Experimental and numerical characterization of magnetophoretic separation for MEMS-based biosensor applications. Biomed Microdevice 12:23–34

Mohamed H, Turner JN, Caggana M (2007) Biochip for separating fetal cells from maternal circulation. J Chromatogr A 1162:187–192

Nagrath S et al (2007) Isolation of rare circulating tumour cells in cancer patients by microchip technology. Nature 450:1235

Nam J, Lim H, Kim D, Jung H, Shin S (2012) Continuous separation of microparticles in a microfluidic channel via the elasto-inertial effect of non-Newtonian fluid. Lab Chip 12:1347–1354

Nam J, Namgung B, Lim CT, Bae J-E, Leo HL, Cho KS, Kim S (2015) Microfluidic device for sheathless particle focusing and separation using a viscoelastic fluid. J Chromatogr A 1406:244–250

Nandy K, Chaudhuri S, Ganguly R, Puri IK (2008) Analytical model for the magnetophoretic capture of magnetic microspheres in microfluidic devices. J Magn Magn Mater 320:1398–1405

Ng AH, Uddayasankar U, Wheeler AR (2010) Immunoassays in microfluidic systems. Anal Bioanal Chem 397:991–1007

Ounis H, Ahmadi G, McLaughlin JB (1991) Brownian diffusion of submicrometer particles in the viscous sublayer. J Colloid Interface Sci 143:266–277

Ozkumur E et al (2013) Inertial focusing for tumor antigen–dependent and–independent sorting of rare circulating tumor cells. Sci Transl Med 5:179ra147

Pappas D (2016) Microfluidics and cancer analysis: cell separation, cell/tissue culture, cell mechanics, and integrated analysis systems. Analyst 141:525–535. https://doi.org/10.1039/c5an01778e

Parrott C (2017) Computational fluid dynamics (CFD) simulation of microfluidic focusing in a low-cost flow cytometer. Oregon State University, Oregon

Podar M et al (2007) Targeted access to the genomes of low-abundance organisms in complex microbial communities. Appl Environ Microbiol 73:3205–3214

Ramadan Q, Christophe L, Teo W, ShuJun L, Hua FH (2010) Flow-through immunomagnetic separation system for waterborne pathogen isolation and detection: application to Giardia and Cryptosporidium cell isolation. Anal Chim Acta 673:101–108

Richardson SD, Ternes TA (2011) Water analysis: emerging contaminants and current issues. Anal Chem 83:4614–4648

Sabaghan A, Edalatpour M, Moghadam MC, Roohi E, Niazmand H (2016) Nanofluid flow and heat transfer in a microchannel with longitudinal vortex generators: two-phase numerical simulation. Appl Therm Eng 100:179–189

Saeed OO, Li R, Deng Y (2014) Microfluidic approaches for cancer cell separation. J Biomed Sci Eng 7:1005

Saffman P (1965) The lift on a small sphere in a slow shear flow. J Fluid Mech 22:385–400

Sajeesh P, Sen AK (2014) Particle separation and sorting in microfluidic devices: a review. Microfluid Nanofluid 17:1–52. https://doi.org/10.1007/s10404-013-1291-9

Saliba A-E et al (2010) Microfluidic sorting and multimodal typing of cancer cells in self-assembled magnetic arrays. Proc Natl Acad Sci 107:14524–14529

Shardt O, Mitra SK, Derksen J (2012) Lattice Boltzmann simulations of pinched flow fractionation. Chem Eng Sci 75:106–119

Telleman P, Larsen UD, Philip J, Blankenstein G, Wolff A (1998) Cell sorting in microfluidic systems. In: Micro total analysis systems' 98. Springer, pp 39–44

Valero A, Braschler T, Demierre N, Renaud P (2010) A miniaturized continuous dielectrophoretic cell sorter and its applications. Biomicrofluidics 4:022807

Wang MM et al (2005) Microfluidic sorting of mammalian cells by optical force switching. Nat Biotechnol 23:83

Wyatt Shields Iv C, Reyes CD, López GP (2015) Microfluidic cell sorting: a review of the advances in the separation of cells from debulking to rare cell isolation. Lab Chip 15:1230–1249. https://doi.org/10.1039/c4lc01246a

Yamada M, Seki M (2005) Hydrodynamic filtration for on-chip particle concentration and classification utilizing microfluidics. Lab Chip 5:1233–1239

Yamada M, Nakashima M, Seki M (2004) Pinched flow fractionation: continuous size separation of particles utilizing a laminar flow profile in a pinched microchannel. Anal Chem 76:5465–5471

Yang BH, Wang J, Joseph DD, Hu HH, Pan T-W, Glowinski R (2005) Migration of a sphere in tube flow. J Fluid Mech 540:109–131

Yang R-J, Hou H-H, Wang Y-N, Fu L-M (2016) Micro-magnetofluidics in microfluidic systems: a review. Sens Actuators B Chem 224:1–15

Yilmaz S, Singh AK (2012) Single cell genome sequencing. Curr Opin Biotechnol 23:437–443

Zhang J, Yan S, Yuan D, Zhao Q, Tan SH, Nguyen N-T, Li W (2016) A novel viscoelastic-based ferrofluid for continuous sheathless microfluidic separation of nonmagnetic microparticles. Lab Chip 16:3947–3956

Zhang J et al (2018) Tunable particle separation in a hybrid dielectrophoresis (DEP)-inertial microfluidic device. Sens Actuators B Chem 267:14–25

Zhou J, Papautsky I (2013) Fundamentals of inertial focusing in microchannels. Lab Chip 13:1121–1132

Zhou Y, Ma Z, Tayebi M, Ai Y (2019) Submicron particle focusing and exosome sorting by wavy microchannel structures within viscoelastic fluids. Anal Chem 91:4577–4584

Zhu T, Lichlyter DJ, Haidekker MA, Mao L (2011) Analytical model of microfluidic transport of non-magnetic particles in ferrofluids under the influence of a permanent magnet. Microfluid Nanofluid 10:1233–1245

Zolgharni M, Azimi S, Bahmanyar M, Balachandran W (2007) A numerical design study of chaotic mixing of magnetic particles in a microfluidic bio-separator. Microfluid Nanofluid 3:677–687